Empirical Return Periods of the Most Intense Vapor Transports during Historical Atmospheric River Landfalls on the U.S. West Coast

MICHAEL D. DETTINGER[a]

U.S. Geological Survey, Carson City, Nevada, and Center for Western Weather and Water Extremes, Scripps Institution of Oceanography, La Jolla, California

F. MARTIN RALPH[b]

Center for Western Weather and Water Extremes, Scripps Institution of Oceanography, La Jolla, California

JONATHAN J. RUTZ[c]

NOAA/NWS/Western Region Science and Technology Integration Division, Salt Lake City, Utah

(Manuscript received 2 January 2018, in final form 12 June 2018)

ABSTRACT

Atmospheric rivers (ARs) come in all intensities, and clear communication of risks posed by individual storms in observations and forecasts can be a challenge. Modest ARs can be characterized by the percentile rank of their integrated water vapor transport (IVT) rates compared to past ARs. Stronger ARs can be categorized more clearly in terms of return periods or, equivalently, historical probabilities that at least one AR will exceed a given IVT threshold in any given year. Based on a 1980–2016 chronology of AR landfalls on the U.S. West Coast from NASA's Modern-Era Retrospective Analysis for Research and Applications, version 2 (MERRA-2), datasets, the largest instantaneous IVTs—greater than 1700 kg m^{-1} s^{-1}—have occurred in ARs making landfall between 41° and 46°N with return periods longer than 20 years. IVT values with similar return periods are smaller to the north and, especially, to the south (declining to ~750 kg m^{-1} s^{-1}). The largest storm-sequence IVT totals have been centered near 42.5°N, with scatter among the top few events, and these large storm-sequence totals depend more on sequence duration than on the instantaneous IVT that went into them. Maximum instantaneous IVTs are largest in the Pacific Northwest in autumn, with largest IVT values arriving farther south as winter and spring unfold, until maximum IVTs reach Northern California in spring.

1. Introduction

Atmospheric rivers (ARs; Zhu and Newell 1998) are naturally occurring, transitory, long (>2000 km), narrow (~850 km) streams of intense water vapor transport through the lower atmosphere (<3 km above sea level; Ralph et al. 2004; Guan and Waliser 2017). ARs over the northeast Pacific conduct massive amounts of water vapor (anywhere from 5 to 25 times the average flow of the Mississippi River into the Gulf of Mexico) through the atmospheric arm of the extratropical water cycle (Ralph and Dettinger 2011), often connecting tropical and extratropical moisture sources to the U.S. West Coast (Cordeira et al. 2013). When these ARs encounter West Coast mountain ranges, they are uplifted and cooled, producing heavy rain and snow (Neiman et al. 2002; Guan et al. 2010), providing 20%–50% of total precipitation in the Pacific Coast states (Dettinger et al. 2011; Rutz et al. 2014).

The most intense ARs produce massive amounts of precipitation on the West Coast states. Among the largest storms in California's history—storms that produced more than 400 mm of precipitation within 3 days—92% have been ARs (Ralph and Dettinger 2012). In large part because of these precipitation totals, ARs have been the dominant cause of historical floods along rivers of the

Denotes content that is immediately available upon publication as open access.

[a] ORCID: 0000-0002-7509-7332.
[b] ORCID: 0000-0002-0870-6396.
[c] ORCID: 0000-0003-4337-0071.

Corresponding author: M. D. Dettinger, mddettin@usgs.gov

DOI: 10.1175/JHM-D-17-0247.1

Pacific Northwest (PNW) and central and northern California (Ralph et al. 2006; Dettinger and Ingram 2013; Neiman et al. 2011; Barth et al. 2017; Konrad and Dettinger 2017), where over 80% of floods since 1950 have been attributable to strong ARs. The most intense ARs have historically caused landslides, debris flows, levee failures, erosion, and consequent societal impacts (Dettinger and Ingram 2013; Florsheim and Dettinger 2015; Oakley et al. 2017; Young et al. 2017; Oakley et al. 2018). At the same time, though, strong landfalling ARs have also brought about the termination from more than 70% of historical droughts in Washington, with AR-induced drought terminations falling off to the south, to about 35% of drought terminations in southern California (Dettinger 2013).

However, not all ARs produce these extreme precipitation and flood conditions. Rather, ARs range between very modest intensities [as measured by the amount of vertically integrated water vapor transport (IVT) that they conduct per meter of cross-sectional distance, in $kg\,m^{-1}\,s^{-1}$] and very strong intensities. The more water vapor that an AR transports, the more precipitation it can yield (e.g., Neiman et al. 2002, 2009; Ralph et al. 2013; Guan and Waliser 2015), depending also on several other characteristics of the storm, including (but not limited to) the orientation of the transports relative to the steepest ascents of the mountain ranges they encounter, stability of the atmosphere, and closeness of air within the AR to saturation with respect to vapor upon landfall. The least intense ARs are unlikely to yield extreme precipitation and are most often beneficial sources of moderate rains, snowfalls, and water resources of Pacific-state landscapes.

Thus, ARs range between largely beneficial and largely hazardous (Ralph et al. 2017a, 2018, manuscript submitted to *Bull. Amer. Meteor. Soc.*), and the intensity of an AR storm—which plays a dominant role in determining where in this range an AR storm will fall—is one of the most important characteristics that must be communicated for forecasts of an AR landfall (Cordeira et al. 2017). A natural way to describe the largest ARs to the public and professionals alike is by comparison to other, historical large ARs and their consequences, much as one often describes or analogizes a current riverine flood and its impacts with some specific past flood. However, many stakeholders do not accurately recall specific historical storms or floods (e.g., "the great storm/floods of New Years 1997"), and so—with some technical misgivings (e.g., Shepard 2015)—riverine floods are categorized in terms of their estimated return periods (or annual probabilities of exceedence) at least as often as by reference to specific historical events.

With this communications issue in mind, this paper analyzes historical IVTs in ARs making landfall on the U.S. West Coast from a global atmospheric reanalysis dataset in terms of simple rank percentiles for small to moderate ARs, and in terms of historical return periods of annual-maximum IVT values. The analysis allows strong ARs, in records and forecasts, to be categorized across the full range of AR intensities in terms of how often ARs of similar intensity have occurred historically, thus allowing a sense of "how intense is this storm compared to all the other ones?" to be communicated in simple, quantitative terms.

2. Data

This analysis proceeds from chronologies of ARs on the U.S. West Coast and their IVTs at landfall, as identified by the application of the method of Rutz et al. (2014) to long-term global atmospheric reanalysis products. These reanalysis products are detailed representations of the state of the global atmosphere based on assimilation of available historical observations into a numerical weather (forecast) model, with the version of that model held fixed throughout the period of the analysis (Ghil and Malanotte-Rizzoli 1991; Kalnay et al. 1996). The reanalysis calculations yield time series of all atmospheric variables and conditions simulated at every grid cell and vertical level in the model, variables, and conditions that are internally and dynamically consistent with each other, with historical observations, and with the model's governing equations. The observations may include surface observations on land and sea, weather balloon and aircraft observations, and satellite imagery to the extent that each source is available at each reanalysis time step.

The reanalysis product that will be the primary focus here is NASA's Modern-Era Retrospective Analysis for Research and Applications, version 2 (MERRA-2), reanalysis (Gelaro et al. 2017; GMAO 2015), using 3-hourly data on its 0.5° latitude × 0.625° longitude grid spanning 37 historical years (or 36 water years, October–September) during the satellite era (1981–2016). Corresponding results from selected segments from two other reanalysis products will be considered in section 4:

- the National Centers for Environmental Prediction–National Center for Atmospheric Research (NCEP–NCAR) Reanalysis-1 (Kalnay et al. 1996, and updates thereto), which spans >65 years (1948–2012 considered here) of historical conditions at 6-hourly time steps on a spatially coarse 2.5° latitude and longitude grid, and
- the part of one of the European Center for Medium-Range Weather Forecasts (ECMWF) interim reanalysis (ERA-Interim; Dee et al. 2011) products used in Rutz et al. (2014), on a 1.5° latitude and longitude grid, on 6-hourly time steps, and spanning 22 years of historical conditions (1989–2010). Notably, ERA-Interim datasets

are available at a variety of different resolutions, including finer than that used herein, and over longer time periods. We use this particular segment of the reanalysis not to suggest that ERA-Interim could not be used in the analyses to follow, but rather to provide a perspective on how the choice of datasets—specifically, the choice of resolutions—affects results of our analyses of MERRA-2 ARs.

Rutz et al.'s (2014) approach to identifying ARs in such datasets evaluates global IVT fields from these reanalysis datasets, with IVT calculated according to the methodologies of Neiman et al. (2008) and Moore et al. (2012) as

$$\mathrm{IVT} = -\frac{1}{g}\int_{p_b}^{p_t} q\mathbf{V}_h\, dp, \qquad (1)$$

where q is specific humidity, $\mathbf{V}_h$ is the horizontal wind vector, g is the acceleration due to gravity, p_b is 1000 hPa, and p_t is 200 hPa. In order for the following comparisons of AR IVTs in the three reanalyses to be as consistent as possible (not all of the reanalyses considered provide internally derived IVTs) and to maintain consistency with previous applications of Rutz et al.'s (2014) method, all IVTs used in this study were calculated from humidities and winds on standard model pressure levels at the standard 3- or 6-h model-output time steps. A useful alternative for future studies might be IVT values that the MERRA-2 system provides directly, which have the advantage that these internally generated IVTs are calculated at all (internal) model times steps and on all model vertical coordinates and not just the standard output pressure levels. In a comparison of instantaneous IVTs from the MERRA-2 datasets by Shields et al. (2018, their Fig. S1), internally derived IVTs did not differ substantially (less than about 1 $\mathrm{kg\,m^{-1}\,s^{-1}}$) from the IVTs used herein. Nonetheless, the internally derived IVTs may be preferable over coasts and mountains in the long run.

At each time step, Rutz et al.'s (2014) method identifies ARs as features in the global IVT fields that are >2000 km in length with IVT > 250 $\mathrm{kg\,m^{-1}\,s^{-1}}$ throughout. In the present study, AR arrivals on the U.S.West Coast identified by application of this algorithm to each time step (separately) in each of the three reanalysis datasets were analyzed, and the IVT values of the ARs as they encounter the West Coast were tabulated and used to characterize the intensity of landfalling ARs. Examples of IVT time series that result from these calculations, along with the water-year maximum IVT values, are shown in Fig. 1, for the MERRRA-2 grid cell at 37.5°N, 123.5°E (offshore from San Francisco Bay, California) and 48.5°N, 126.25°W (offshore from the northern tip of the Olympic Peninsula in Washington). In both series, annual-maximum IVT values range from about 750–800 $\mathrm{kg\,m^{-1}\,s^{-1}}$ to about 1300–1400 $\mathrm{kg\,m^{-1}\,s^{-1}}$, with considerable year-to-year variation and modest, if any, trends or steps. (Trend and changepoint analyses will be described briefly in the next section.)

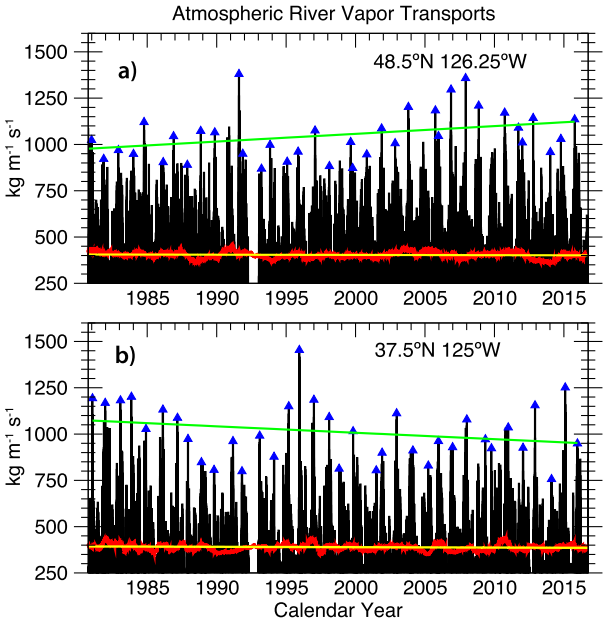

FIG. 1. Vertically integrated 3-hourly water vapor transports during atmospheric river conditions (black bars) over the MERRA-2 grid cell at (a) 48.5°N, 126.25°W and (b) 37.5°N, 125°W for the period from 1 Oct 1980 through 30 Sep 2016; the red curve is a 365-day moving average of 3-hourly values, yellow and green lines are linear regression fits to all-AR IVTs and water-year maximum AR IVTs, and blue triangles are water-year maximum IVT values.

These AR chronologies are Eulerian in character in that individual ARs are not followed, as moving features, through space and time. Instead AR conditions overhead are identified and tabulated for each of the grid cells closest to the West Coast. In this sense, the term "AR storm sequence" used in later sections of this paper refers to periods when AR conditions are continuously present overhead of the grid cell in question, and not the life cycle of an individual AR moving through the atmosphere.

3. Analysis approach

An example analysis of IVTs in all ARs making landfall at selected latitudes along the U.S. West Coast from 1980 to 2016, as identified in the MERRA-2 dataset, is summarized in Table 1, which lists percentages of time that an AR with intensity surpassing various thresholds has made landfall at selected latitudes along

TABLE 1. Percentages of historical nonoverlapping 3-day periods with at least one AR landfall with 3-hourly IVT maxima greater than the indicated thresholds, in MERRA-2 fields, calendar years 1980–2016.

	IVT thresholds					
Landfall latitude	325 kg m^{-1} s^{-1}	500 kg m^{-1} s^{-1}	625 kg m^{-1} s^{-1}	750 kg m^{-1} s^{-1}	875 kg m^{-1} s^{-1}	Maximum reported
49°N	80%	38%	19%	9%	4%	1333 kg m^{-1} s^{-1}
47°N	79%	41%	23%	12%	5%	1552 kg m^{-1} s^{-1}
45°N	81%	45%	27%	15%	8%	1730 kg m^{-1} s^{-1}
43°N	80%	45%	27%	16%	8%	1619 kg m^{-1} s^{-1}
41°N	78%	38%	20%	10%	2%	1483 kg m^{-1} s^{-1}
39°N	74%	32%	17%	8%	4%	1299 kg m^{-1} s^{-1}
37°N	71%	30%	14%	6%	3%	1400 kg m^{-1} s^{-1}
35°N	67%	25%	11%	5%	2%	1244 kg m^{-1} s^{-1}
33°N	62%	21%	7%	2%	0.4%	879 kg m^{-1} s^{-1}

the U.S. West Coast. Maximum IVTs during nonoverlapping 3-day periods were evaluated here in order to avoid double counting IVTs from the same ARs (based on typical lengths of AR landfalls over sites along the U.S. West Coast; Ralph et al. 2013). Among identified ARs, maximum IVTs were between 250 kg m^{-1} s^{-1} [the minimum IVT for inclusion as an AR in Rutz et al.'s (2014) methodology] and 500 kg m^{-1} s^{-1} from 50% to 70% of the time, depending on landfall latitude. Maximum IVTs are greater than 875 kg m^{-1} s^{-1} between 2% and 8% of the time, with most such exceedences occurring along the Northern California and Oregon coasts. This configuration of IVTs generally reflects the patterns of long-term mean and 95th percentile IVT over the northeast Pacific Ocean described by Lavers et al. (2015), wherein maximum IVT values have historically been focused along a line connecting 30°N just south of Japan to somewhere near 45°N on the West Coast, with IVTs declining otherwise to the north and south.

Notably, for ARs with the strongest IVTs, the landfalls reported in Table 1 are so infrequent that the communications value of comparing ARs in terms of IVT percentiles is reduced (e.g., how does one convey the difference between a 2% and 3% storm?). Consequently, for stronger ARs, which are the focus of this study, we draw lessons from the methods typically used to characterize the largest riverine floods. We thus focus on return periods, which are generally more intuitive to a nonscientific audience. Return periods account better for year-to-year variations in AR frequencies than do period-of-record percentiles. Return periods are also a common descriptor in engineering and planning designs, for example, in the form of "100-yr storms" and other categorizations of risk and intensity.

Thus, in the remainder of this study, empirical estimates of the return periods of ARs exceeding various strong-AR IVT thresholds are quantified as a means for communicating the strength of the largest AR storms that have made landfall on the U.S. West Coast in recent decades. The return periods are estimated from the time series of annual-peak IVTs during landfalling ARs at each landfall latitude (e.g., as in Fig. 1). First, for each water year in a reanalysis dataset, the maximum 3- or 6-hourly IVT value associated with an AR making landfall at a given latitude or latitude band is identified. Then these annual-peak IVTs are ranked, with a standard "plotting position" (rank divided by $N + 1$, where N is the length of the time series; Makkonen 2006), and herein each annual maximum is then plotted with its plotting position located along a normal distribution on the x axis and its IVT value generally plotted along a logarithmic scale on the y axis. Other plotting/estimation approaches could have been used, so that the lognormal plotting of the IVT maxima here is somewhat arbitrary. However, Table 2 compares regression fits when simple or logarithmic plotting-position probabilities, normal or lognormal probabilities, and Pearson type III or log-Pearson type III probabilities are used. The table shows that all of the distributions provide reasonable fits across the historical ranges of annual-maximum IVT values. Our purpose here is not to provide parametric estimates of return periods for extrapolations beyond the historically observed range of values (to, e.g., 100-yr storms well beyond our 22–65-yr-long records), but rather to provide broad empirical estimates of return periods for everyday communication purposes. The identification of the most appropriate parametric distributions (Carpenter and Bithell 2000) for extreme events analysis of IVTs (as opposed to floods in surface rivers) is a project for the future, and thus even the confidence limits that are presented later are based on nonparametric bootstrap resamplings of the observed IVT values. For engineering and extrapolation purposes, much more intensive, precise, and application-specific choices and fits of extreme-value distributions (Interagency Advisory Committee on Water Data 1982) will presumably be needed.

Calculated this way, the resulting return periods (or recurrence intervals) are estimates of the inverse of the

TABLE 2. Coefficients of determination (regression r^2) of annual-maximum 3-hourly IVT values during ARs, water years 1981–2016, in MERRA-2 AR chronology at selected West Coast landfall latitudes, for return-period fits vs simple plotting-position odds [rank/(36 + 1)], normal probabilities, and Pearson type III probabilities, and logarithms of the IVTs vs the same three sets of probabilities. All fits are statistically strong ($p \ll 0.0001$) and all yield similar return-period estimates within the historical range of IVT maxima.

Landfall latitude	Odds vs IVT	Odds vs log(IVT)	Normal probs vs IVT	Normals vs log(IVT)	Pearson probabilities vs IVT	Pearson probabilities vs log(IVT)
35°N	96%	97%	97%	98%	97%	99%
40°N	95%	97%	97%	99%	98%	99%
45°N	78%	84%	86%	86%	91%	93%

probability that a given IVT intensity will be equaled or exceeded in any given year. This attention to the largest IVT values each year allows us to focus on characterizing just the largest and most hazardous ARs, without ''dilution'' by the differing numbers of modest ARs at the various latitudes or by occasions when multiple strong ARs arrive in some years.

4. Choice of reanalysis dataset

As noted previously, reanalysis datasets available to identify and characterize AR landfalls differ in their spatial resolutions and in their periods of record. To estimate long-term frequencies, or probabilities, of the strongest historical ARs, a longer record (larger sample size) is generally much preferred. But how does the spatial resolution of a given reanalysis dataset impact the maximum IVTs reported? That is, are maximum IVTs blurred and muted in a lower-resolution product compared to those in a higher resolution dataset? If so, then the higher-resolution dataset might be needed even if its period of record is smaller than a coarse resolution but longer alternative.

Before reporting and discussing return periods of AR intensities in the MERRA-2 chronology (which became the focus of this study), AR IVTs and annual-maximum AR IVTs in the MERRA-2 were compared to those in the longer but coarser Reanalysis-1 AR chronology. These comparisons were made to provide a sense of the effects of coarsening spatial resolutions on reported IVT values and on estimated AR-IVT return periods. To improve further our sense of the effect of grid scale on reanalysis IVT values, a short but intermediate-resolution AR chronology used by Rutz et al. (2014) and based on a part of ERA-Interim is also included in this comparison.

First, IVT values for every 6-hourly time step during a 22-yr period (1989–2010) that was available in all three of the AR chronologies were compared at three grid cells near the U.S. West Coast. Six-hourly values were used because this was the finest temporal resolution common to all three reanalysis chronologies. Grid cells were chosen to be as close to each other as possible (near or at 35°, 40°, and 45°N), which meant choosing grid cells closest to the 2.5° Reanalysis-1 grid cells just offshore at those latitudes (Fig. 2a). Figure 3 compares IVT values from the three reanalyses during every 6-hourly time step in the 22-yr period that coincided with AR conditions in the MERRA-2 AR chronology. At each latitude, AR IVTs for the three chronologies tend to be very similar to each other for the AR time steps with weak to modest IVT intensity (as indicated by comparisons of the dashed one-to-one lines to the regression lines in each panel of Fig. 3). For time steps with more intense ($>500\,\mathrm{kg\,m^{-1}\,s^{-1}}$) AR conditions, the coarser reanalyses yield lower IVT values. The slopes of each of the regression lines in Fig. 3 are significantly less than a one-to-one relation with the MERRA-2 IVT values, suggesting that, when addressing strong IVTs, the spatial resolution of the reanalysis used to characterize ARs matters. The finer MERRA-2 resolution yields IVT values that are roughly about 25% higher than the coarser reanalyses.

Five subsets from the three reanalysis chronologies were also analyzed to compare estimates of return periods at the grid cells nearest those just offshore in Reanalysis-1:

1) Return periods were estimated from the full 65-yr Reanalysis-1 AR chronology spanning the 1948–2012 period.
2) Then return periods were re-estimated from the same chronology but using only values from the 22-yr 1989–2010 period spanned by the shorter ERA-Interim chronology.
3) Return periods were estimated from those 22 years of ERA-Interim AR chronology.
4) Return periods were estimated using a 6-hourly resampling of the 3-hourly MERRA-2 AR chronology during its full 37-yr period of record.
5) Finally, MERRA-2 return periods are estimated based on only ARs during the shorter 22-yr ERA-Interim period.

This comparison of return-period estimates using the various reanalysis chronologies and various periods of

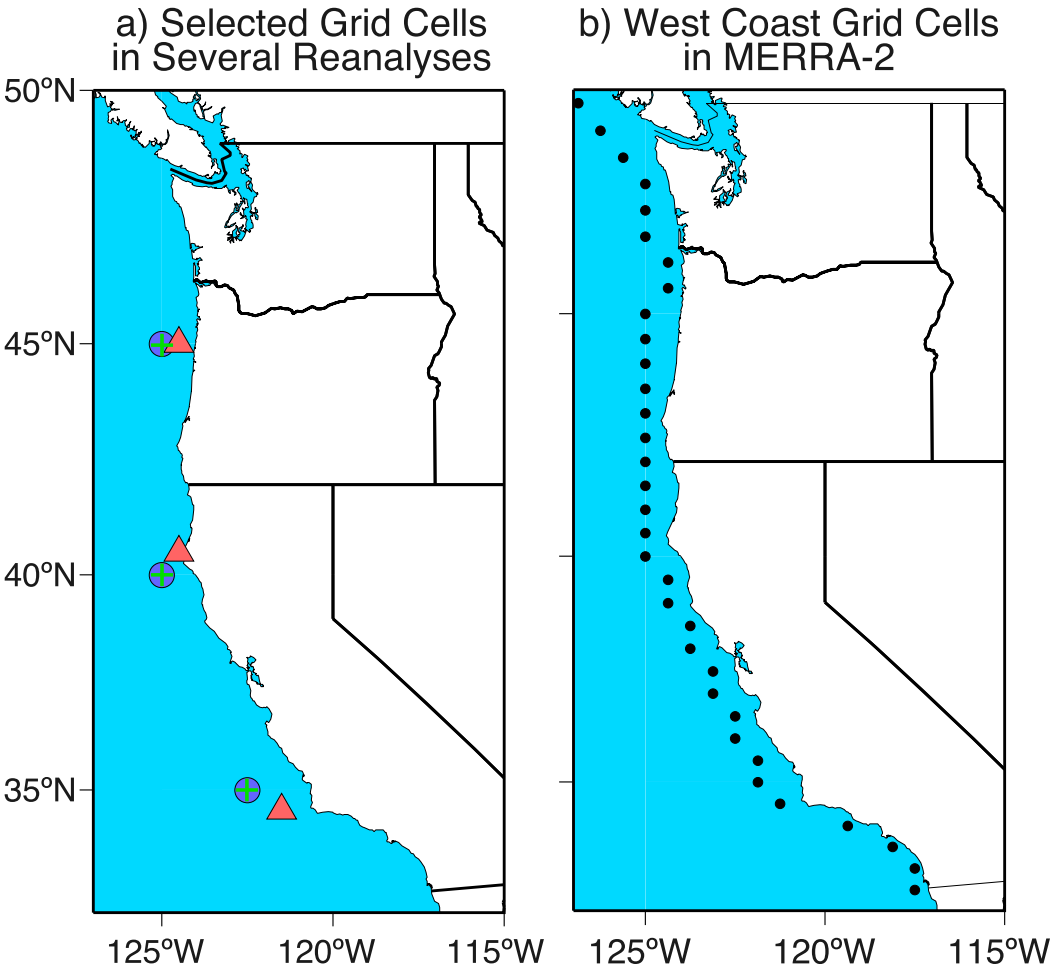

FIG. 2. (a) Centers of grid cells in Reanalysis-1 and MERRA-2 datasets (blue dots and green pluses) and nearest-neighbor ERA-Interim (red triangles) IVT return-period analyses compared in Figs. 3 and 4; (b) centers of MERRA-2 grid cells where annual-maximum IVTs will be explored later in this paper.

record allowed some of the effects of different reanalysis resolutions and different reanalysis time spans on return-period estimation to be directly compared.

The comparisons of annual-maximum IVTs during landfalling ARs shown in Fig. 4a illustrate small differences between return period estimates based on the Reanalysis-1 and ERA-Interim at 45°N, suggesting that the 1.5° resolution of the latter does not substantially alter estimates of the annual-maximum IVT values relative to those from the former with its 2.5° resolution. There are notable differences between return periods estimated from the full 65-yr Reanalysis-1 and the short segment of ERA-Interim (Fig. 4b) among the rarer, but not more frequent, values in the two time periods. To be specific about what we judge to be "good" comparisons, we note the overlaps (and lack thereof) between the various confidence bands [estimated by a bias-corrected and accelerated (BCa) bootstrap resampling (Carpenter and Bithell 2000) of the values of the reanalysis annual-maximum IVT values indicated by the symbols in each panel] and the placement of the IVT observations (symbols) within the respective confidence bands, as well as the fact that the differences arising between the return periods at the various latitudes are generally small compared to the latitude-to-latitude differences, which we will explore in the next section. Farther south at 40°N (Fig. 4c), there is more divergence between return periods from the longer Reanalysis-1 and shorter ERA-Interim, but again the full Reanalysis-1 and ERA-Interim results (Fig. 4d) generally are in good agreement.

However, in all panels of Fig. 4, the green pluses and green confidence bands tend to plot consistently higher than the other symbols and bands (with exception of the longest return periods at 40°N when all three reanalysis are limited to the shorter 22-yr ERA-Interim time span;

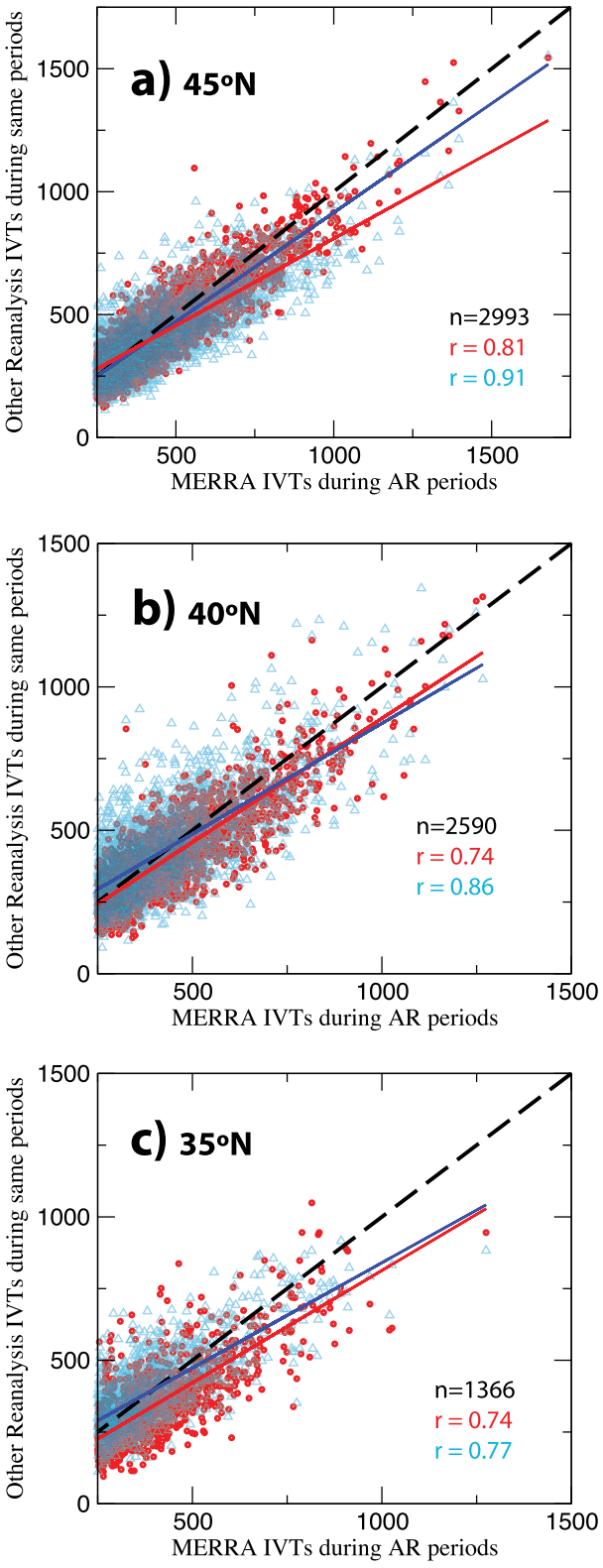

FIG. 3. Comparisons of IVTs in the MERRA-2, Reanalysis-1, and ERA-Interim AR chronologies, during every 6-hourly time step from 1989 to 2010 with AR conditions reported in the MERRA-2 AR chronology at three grid cells shown in Fig. 2a. Red circles are comparisons of IVT values in Reanalysis-1 to MERRA-2, blue triangles (plotted in front of red dots) compare IVTs in ERA-Interim to MERRA-2; and red and blue lines are linear regression fits to red dots and blue triangles, respectively, with correlations for each fit indicated. Dashed black lines indicate one-to-one relations.

Fig. 4c). Thus, comparisons of the IVT return periods from more highly resolved MERRA-2 ARs to the corresponding Reanalysis-1 and ERA-Interim IVTs in Fig. 4 show that IVTs in the higher-resolution MERRA-2 chronology are generally and, in many cases, statistically significantly (at 90% confidence level) higher at most return periods at all three latitudes than in in the more coarsely resolved Reanalysis-1 and ERA-Interim. These higher MERRA-2–derived IVT values are common for all the latitudes north of about 32.5°N (not shown here) and become increasingly so the farther north the landfall latitude.

The systematic tendency for IVT extremes to reach higher IVT values in the higher-resolution MERRA-2 dataset compared to the lower, subdued (smoothed) values in the coarser Reanalysis-1 and ERA-Interim prompts our choice of the medium length (37 years) but high-resolution MERRA-2 chronology as the focus of the remaining sections (and Table 1). Figures 3 and 4 suggest that using the other reanalysis datasets would have resulted in estimates of longer return periods (than reported here) for any specified AR IVT. Our most immediate interest here is communicating AR hazards from operational forecasts, which currently are made at a variety of resolutions: for example, the NCEP Global Forecast System (GFS) forecast model used to calibrate the National Weather Service's Hydrologic Ensemble Forecast System has a 0.5° spatial resolution and the particular time period used for those calibrations is 1980–2106 (Brown et al. 2014; https://www.ncdc.noaa.gov/data-access/model-data/model-datasets/global-forcast-system-gfs). In view of this interest in communicating about modern forecasts, and because the 37-yr MERRA-2 period is adequate to estimate return periods as long as about 20 years fairly accurately, in the remainder of this paper, we analyze and report AR return periods based on the 1980–2016 MERRA-2 AR chronology.

Before proceeding to those analyses, it is worth considering the possibility that the reanalyses used here to characterize AR IVTs might harbor systematic errors. Thus, let us briefly consider the following questions: How do reanalysis IVTs compare to IVTs in the real world? Are there nonstationarities within the reanalysis

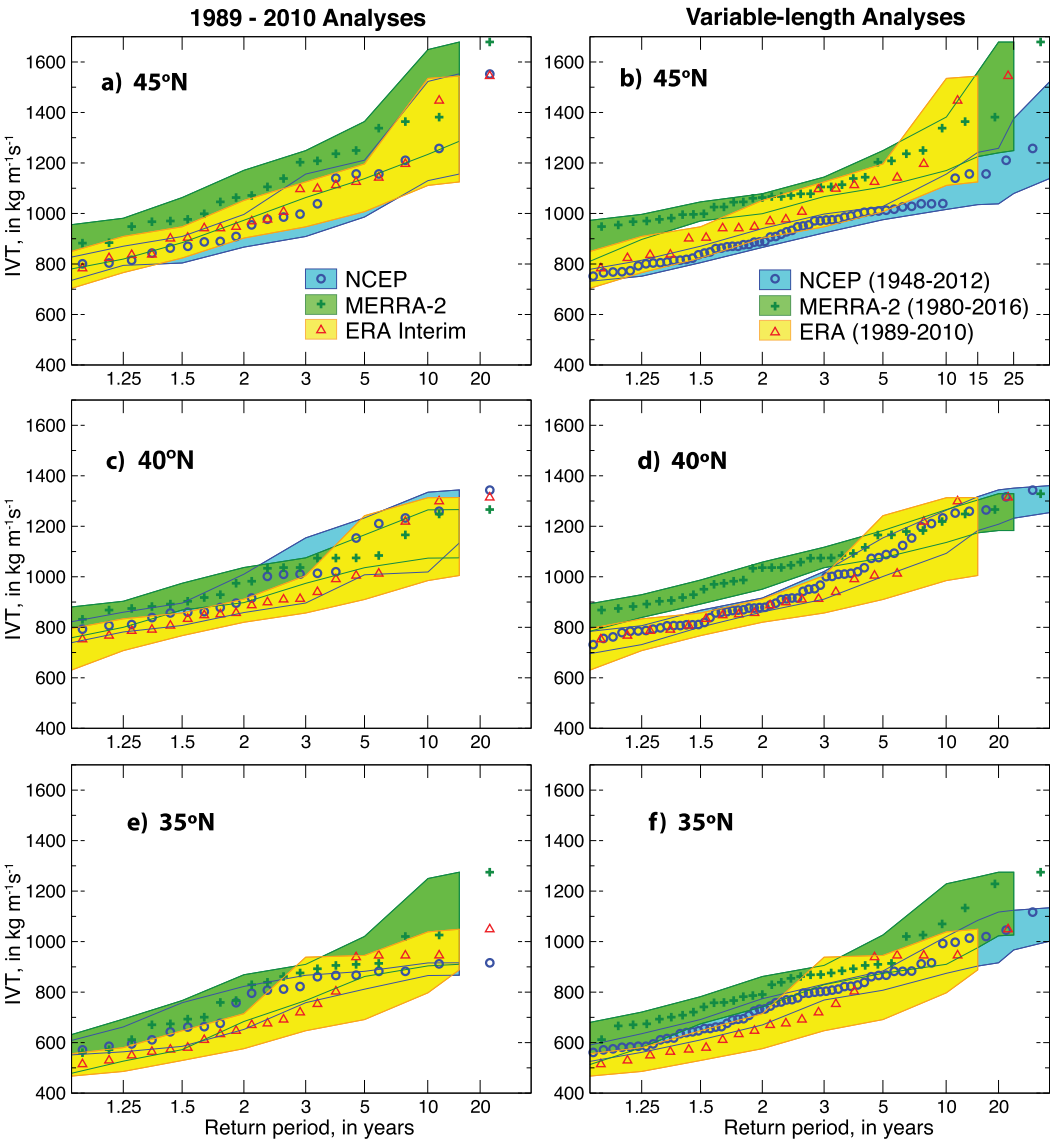

FIG. 4. Comparisons of return-period estimates of annual-maximum 6-hourly IVTs in landfalling ARs, based on (a),(c),(e) the 22-yr period from 1989 to 2010 and (b),(d),(f) full-chronology periods [indicated in (b)], from AR chronologies for three reanalyses, at three grid cells along the U.S. West Coast (Fig. 2a). Symbols are the reanalysis IVT estimates at each return period; color bands are the 90% confidence limits for each based on BCa resampling of the return periods. In order to accommodate overlapping confidence bands, the outer edges of each color band are presented as thin curves in a slightly darker hue.

datasets that would invalidate temporal analyses? First, several recent studies have made comparisons of ARs depicted in reanalysis datasets with direct airborne measurements of these storms in order to document the validity of reanalysis AR properties (Guan and Waliser 2017; Ralph et al. 2017b; Guan et al. 2018). Taken together, based on the 21 dropsonde-observed ARs between 1998 and 2016, these studies conclude that reanalysis IVTs are generally accurate with mean errors less of −1% in MERRA-2 (+3% in ERA-Interim). This result validates the use of ARs detected in reanalysis datasets and the IVT values in those reanalyses.

Despite these encouraging checks on reanalysis IVTs, reanalyses are known to harbor discontinuities associated with changes in the sources (types, provenances, spatial densities, and temporal frequencies) of data input to the reanalysis procedures [e.g., as reported in Gelaro et al. (2017) for MERRA-2, in Dee et al. (2011) for ERA-Interim, and as implied by the major input changes between the presatellite era and satellite era in

Reanalysis-1 of Kalnay et al. (1996)]. Such discontinuities could violate one of the assumptions underlying quantitative estimates of return periods, that is, that the series analyzed are statistically stationary (e.g., Interagency Advisory Committee on Water Data 1982). To evaluate the range of discontinuities present in the datasets used here, tests were performed to detect possible changepoints in 5-yr mean IVTs during all AR landfalls in the MERRA-2 AR chronology. These series are erratic enough, and interannually variable enough (Fig. 1), so that many *possible* changepoints were detected at 95% confidence level. However, the scales of these potential discontinuities were uniformly small in the study domain, from 32.5° to 49.5°N, with 5-yr mean changes large enough to be possible changepoints, averaged at each latitude, ranging between -6 and $+4\,\mathrm{kg\,m^{-1}\,s^{-1}}$ (from -1.4% to $+0.9\%$ change) depending on latitude, and the maximum 5-yr mean changes at the various latitudes falling between -40 and $+40\,\mathrm{kg\,m^{-1}\,s^{-1}}$ ($\pm 10\%$). Similar tests for changepoints in 5-yr variances (Levene 1960) of AR IVTs were also performed; the largest potential changepoints among 5-yr standard deviations ranged from $\pm 45\,\mathrm{kg\,m^{-1}\,s^{-1}}$ at any latitude in the present study domain. Thus, although subtle discontinuities are likely present in reanalysis IVTs, they appear to be small (in MERRA-2) compared to the range of annual-maximum IVTs that will be analyzed here.

However, another kind of nonstationarity—a long-term trend—is now known to be present in historical AR IVTs on the West Coast. Gershunov et al. (2017) describe a long-term trend in West Coast IVTs identified in the NOAA Twentieth Century Reanalysis (Compo et al. 2011), with increasing IVT and precipitation to the north along the West Coast and declines to the south, apparently tied to long-term warming of the tropical Western Pacific and a poleward migration of storm tracks. Figure 5 illustrates trends in the MERRA-2 3-hourly and annual-maximum IVT values series at all of the West Coast grid cells (locations in Fig. 2b) that are the primary focus of this paper. When all AR landfalls are analyzed, overall trends are extremely small in magnitude, but in the annual-maximum IVT series, the overall trends range from -120 to $+150\,\mathrm{kg\,m^{-1}\,s^{-1}}$ along the West Coast. Only at 48.5°N does this change rise to a level that would pass a two-sided 95% significance test amidst the large year-to-year variability in these maximum IVTs (e.g., see Fig. 1a). Nonetheless, the fitted trends in Fig. 5 are quite coherent with latitude and are large enough in magnitude to suggest that they are present. The estimated magnitude of the trend recommends that return periods for annual-maximum IVT estimated here may err by ± 100–$150\,\mathrm{kg\,m^{-1}\,s^{-1}}$, or roughly 10%.

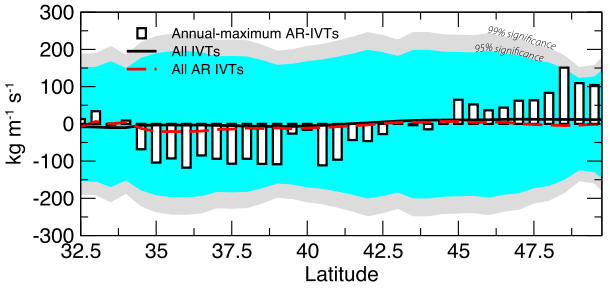

FIG. 5. Overall linear trends in annual-maximum IVTs during AR landfalls (bars), at any time (black curve), and during any AR landfalls (dashed red curve), as a function of West Coast latitude (locations shown in Fig. 2b), in MERRA-2 AR chronology, 1980–2016. Overall trends are differences in linearly regressed IVTs at the beginning of 1980 and at the end of 2016. A null hypothesis that the maximum-annual IVT trends falling within the cyan and gray bands are different from zero cannot be rejected at 95% and 99% levels, respectively.

5. Geography of AR return periods

Focusing then on the full 3-hourly, 0.5° latitude × 0.625° longitude, MERRA-2 dataset and AR chronology for water years 1981–2016, Fig. 6 shows empirical estimates of return periods of annual-maximum AR IVT values at six locations (from among the grid cells in Fig. 2b) and in four latitude bands along the U.S. West Coast. On a latitude-by-latitude basis (Figs. 6a,b), north of about 37.5°N, landfall IVTs associated with the range of return periods shown fall within a relatively narrow range of values, although within that band IVTs at 45°N are consistently the largest shown. Generally though, north of about 37.5°N, an annual-maximum IVT value of about $1000\,\mathrm{kg\,m^{-1}\,s^{-1}}$ is exceeded every 1.5–2 years, and annual-maximum values greater than about $1250\,\mathrm{kg\,m^{-1}\,s^{-1}}$ occur about every 7 years. From 37.5°N southward to 32.5°N, annual-maximum IVT values fall off quickly, so that at 32.5°N, a maximum-annual IVT value with 1.5-yr return period is only $600\,\mathrm{kg\,m^{-1}\,s^{-1}}$ and a 20-yr annual-maximum IVT is still less than $1000\,\mathrm{kg\,m^{-1}\,s^{-1}}$.

The solid curves in Fig. 6c show return periods for annual-maximum IVTs during AR landfalls anywhere within four latitude bands along the West Coast. The solid black curve shows return periods for AR landfalls occurring anywhere along the West Coast in any given year, whereas the solid blue curve shows return periods for AR landfalls anywhere between 42° and 50°N (roughly anywhere along the Oregon or Washington coast lines). Because, as noted previously, the largest IVT maxima have occurred at and around 45°N, these two curves (blue and black) are very similar. Annual-maximum IVTs along the Northern California coast (green curve) are generally about 10% lower than those

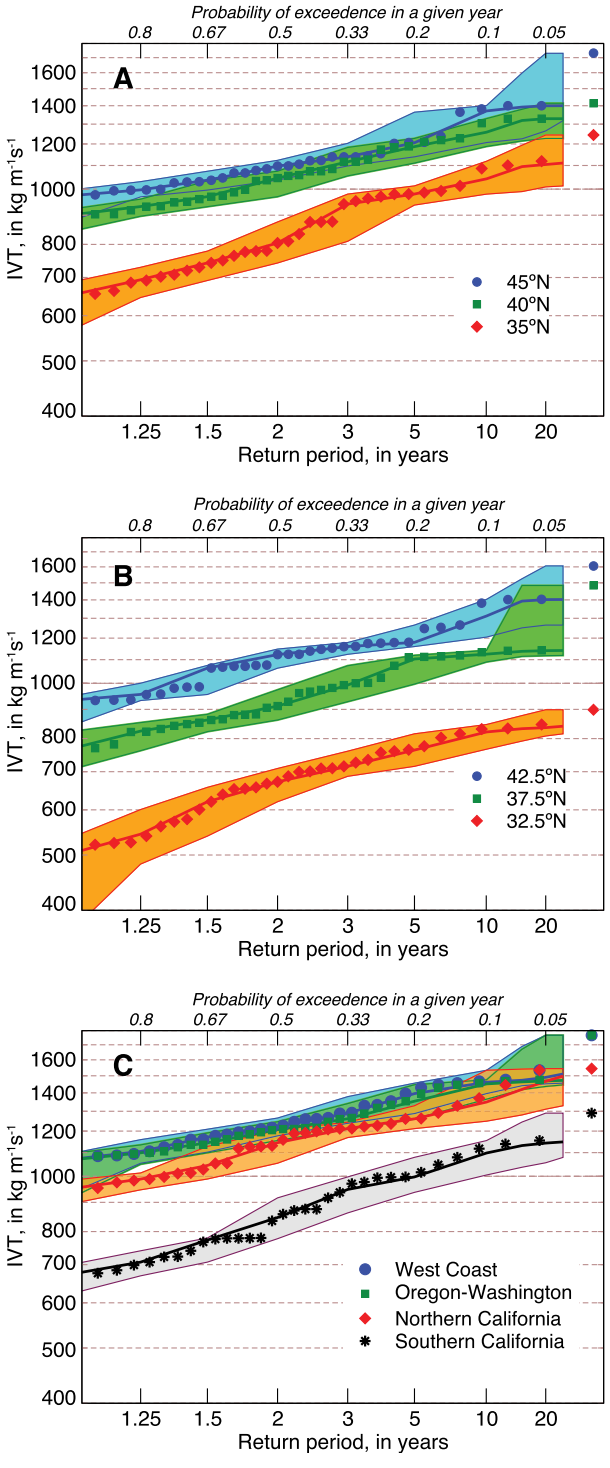

FIG. 6. Historical return periods (and probabilities of exceedence) and confidence bands of water-year annual-maximum AR rates of IVT in 3-hourly periods at selected (a),(b) latitudes and (c) latitude bands along the U.S. West Coast (from among the black dots on maps in Fig. 2b), based on MERRA-2, water years 1981–2016. Symbols are MERRA-2 annual-maximum IVT values; color bands represent the 90% confidence limits from BCa bootstrap resampling (as in Fig. 4), with upper and lower limits indicated by thin curves (at the same return periods) along the Oregon–Washington coast. Annual-maximum IVTs along the Southern California coast (red curve) range from 30% to 40% less than the other bands and echo the values at the northern limits of this band, for example, at 35°N.

A more complete representation of the geographic distribution of annual-maximum IVT return periods is shown in Fig. 7a. As in Fig. 6 and in general accordance with the historical patterns of IVT over the northeast Pacific shown by Lavers et al. (2015), the largest annual-maximum West Coast IVT values encountered have occurred near 45°N (palest pink area in Fig. 7a) with values greater than 1700 kg m^{-1} s^{-1}. Annual-maximum IVT values with largest return periods (~20 years) decline to the north and south. IVT values with much shorter return periods (e.g., ~1.5 years) are, of course, much smaller (<1000 kg m^{-1} s^{-1}) everywhere but also obtain the largest values near (just south of) 45°N. At the southernmost latitudes shown in Fig. 7a, IVT values with roughly 1-yr return periods are less than 500 kg m^{-1} s^{-1}.

6. Storm-sequence vapor-transport total return periods

The maximum instantaneous (3-hourly) IVT values discussed thus far can give indications of resulting maximum precipitation intensities (Neiman et al. 2002, 2009; Ralph et al. 2013; Guan and Waliser 2015), which are relevant to predictions of flood or inundation peaks in some small catchments and to some erosion and Earth-movement processes and risks. For flood prediction in even moderately large catchments and other hazards, though, duration of an AR landfall and precipitation over a given location can be at least as important (Ralph et al. 2013; Lamjiri et al. 2017). Thus, another metric that is now used to characterize ARs is the time-integrated storm-sequence total-IVT amount [measured in kg m^{-1}; paralleling storm-total strategies used by Ralph et al. (2013) and Lamjiri et al. (2017)] at a given location. In this analysis, these storm totals are computed, in an Eulerian sense, as the time-integrated IVT total that passes overhead of the location during each time period (storm) when AR conditions continuously are present above that location. For the very large AR "storm" totals considered here, which include durations as long as 6 days, these uninterrupted AR

←

along with bootstrapped estimates of median return periods indicated by a third (central) curve. In (c), West Coast band spans 32.5°–50°N; Oregon–Washington, 42.5°–50°N; Northern California, 36°–42°N; and Southern California, 32.5°–35.5°N.

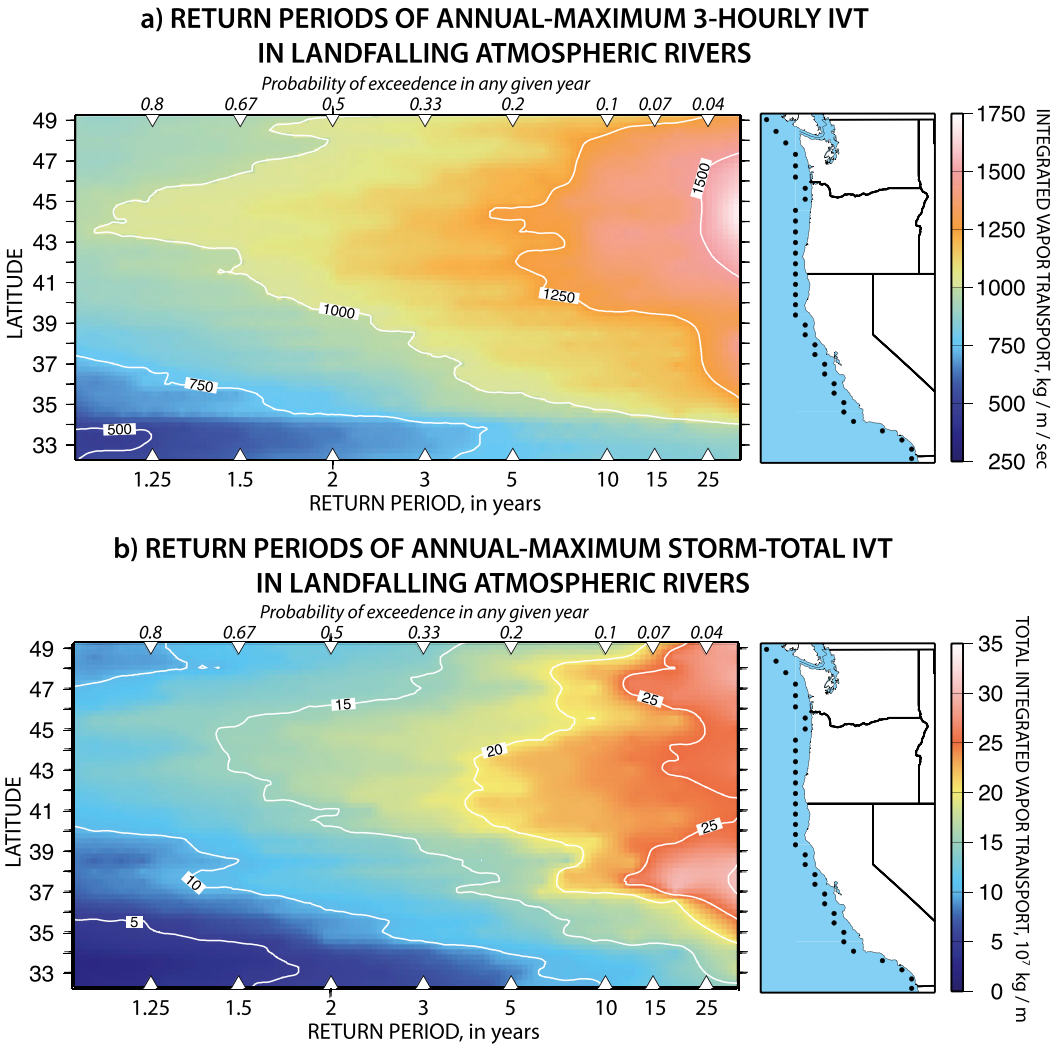

FIG. 7. Historical return periods (and exceedence probabilities) of (a) annual-maximum IVT transport rates and (b) annual-maximum storm totals in landfalling ARs, water years 1981–2016, along the U.S. West Coast at grid cells indicated by black dots in maps along right-hand side of the panels, based on MERRA-2.

conditions almost certainly do not represent a single AR arrival but rather are likely to consist of storm sequences of multiple ARs.

Figure 7b shows the geographic distribution along the U.S. West Coast of return periods of annual-maximum storm-sequence total-IVT amounts. Unlike instantaneous IVT (with its observed maximum near 45°N), the largest West Coast annual-maximum AR storm-total IVT values in the MERRA-2 chronology ($>30 \times 10^7\,\mathrm{kg\,m^{-1}}$ with return period >20 years) have historically occurred near 37.5° and 47.5°N. Notably, this double-peaked distribution of 20-yr storm-total IVTs is restricted to the large, rarest storm sequences, and so may reflect scatter associated with the limitations of estimating 20-yr return periods using time series only 37 years long. To test this interpretation, a similar analysis (not shown) was made of the 65-yr-long Reanalysis-1 AR chronology discussed in section 4. With that longer time series, storm sequences with return periods of 10–30 years are better sampled, and the double-peaked distribution for these larger, rarer storm sequences does not emerge. Instead, the peak near 37.5°N remains but the apparent peak at 47.5°N disappears when 28 more years are included in the analysis.

For storm totals with return periods less than about 5 years, the storm-total maxima are largest near 42°–45°N (Oregon coast), with 1.25-yr storm totals rising to about $12 \times 10^7\,\mathrm{kg\,m^{-1}}$ there and with the smallest 1.25-yr values occurring at the southern limit of this analysis where 1.25-yr IVT values decline to $<2 \times 10^7\,\mathrm{kg\,m^{-1}}$.

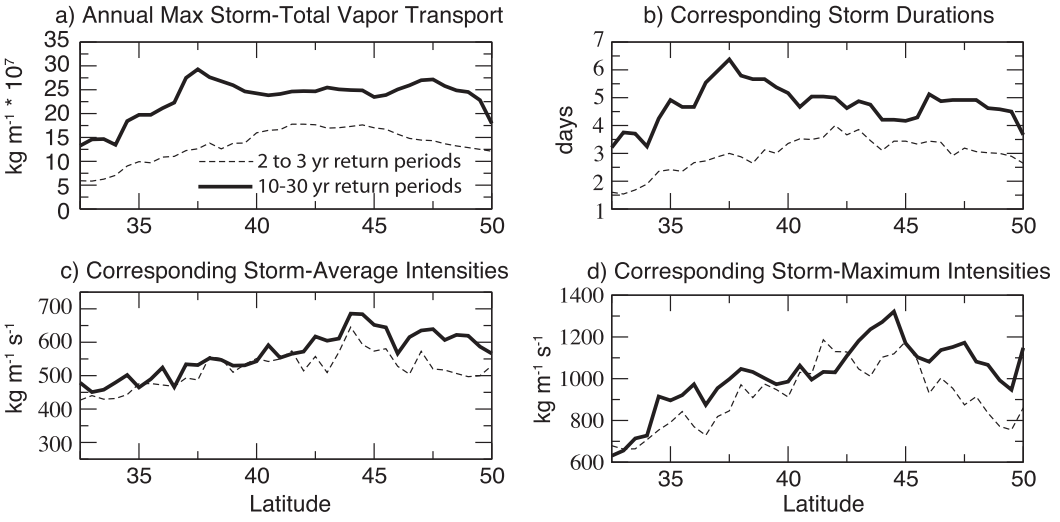

FIG. 8. Latitudinal distribution of (a) the annual-maximum storm-sequence total vapor transport with return periods from 2 to 3 years and from 10 to 30 years, (b) the duration of these same storm sequences, (c) the average IVT over the entire storm sequence, and (d) the maximum instantaneous IVT during the storm sequence, for ARs or uninterrupted sequences of ARs making landfall along the U.S. West Coast, water years 1981–2016.

The durations and IVT rates that combine to yield these large return-period storm sequences are illustrated in Fig. 8. Figure 8a shows IVT totals mapped in Fig. 7b, as averaged over return-period bands from 2 to 3 years and from 10 to 30 years. The double peak noted earlier in Fig. 7b for the longest return-period storm sequences is evident in Fig. 8a, as is the simpler geographic distribution for shorter return periods. For each annual-maximum storm sequence that contributed to Figs. 7b and 8a, durations, storm-maximum IVT rates, and IVT averaged over the entire storm sequence are shown in Figs. 8b and 8c, respectively. Storm-average IVT rates are more or less the same (with ±10% scatter) between sequences with 10–30-yr and 2–3-yr return periods from 32.5° to 42°N, with large storm sequences north of 42°N exhibiting 10%–20% larger average intensities (Fig. 8c). At most latitudes, the maximum instantaneous-IVT rates during the storm sequences with >10-yr return periods are mostly modestly (10%–30%) stronger than those in sequences with 2–3-yr return periods (Fig. 8d). Durations of the >10-yr return-period sequences range from 25% (at 42.5°N) to 140% (33°N) longer than durations of the storm sequences with 2–3-yr return periods (Fig. 7b). The peak in 10–30-yr IVT totals near 37.5°N results from several very long-duration storm sequences (also found in the Reanalysis-1), whereas the apparent peak near 47.5°N (not substantiated by analysis of the Reanalysis-1) arose from a combination of larger storm-average IVT and perhaps some longer-duration sequences there. Overall, though, almost all of the increase in storm-sequence IVT totals with long return periods, which range from 40% to 150% larger, over the storm sequences with shorter return periods arise from differences in their respective durations (see also Lamjiri et al. 2017).

7. Seasonality of AR return periods

The ARs associated with these annual-maximum IVTs make their landfalls at different times of year. To illustrate the seasonality of the AR IVT maxima, Fig. 9 shows return periods of IVT maxima as a function of month and latitude. Thus, the first column in Fig. 9a shows the instantaneous IVT values that would be exceeded, on average, once in every 20 Septembers at each latitude along the U.S. West Coast, the second column for once in every 20 Octobers, and so on. Figure 9b highlights similar results, but for IVTs with 5 September return periods, 5 October returns, and so on. Summer AR IVTs are not shown here because, as documented by Neiman et al. (2008) and acknowledged by many subsequent studies (e.g., Rutz et al. 2014), summer IVT features that are AR-like do not generally produce significant rainfall in the western United States.

The geographic patterns of IVT seasonality are broadly similar for the two panels in Fig. 9, with—for a given return period—largest annual-maximum IVT values arriving in early autumn in the PNW (north of about 43°N, north of California). The maximum IVT values then occur farther south as winter approaches and arrives. By midwinter (December–January), the 20-yr IVT maxima (Fig. 9a) are largest between about 40° and 43°N, and then the locations of the maximum IVT values drift southward

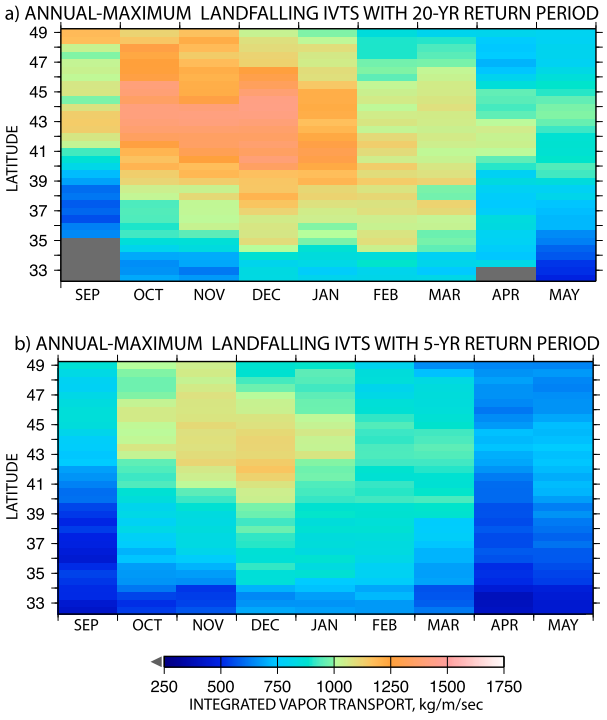

FIG. 9. Annual-maximum 3-hourly IVT rates in landfalling ARs with (a) 20-yr and (b) 5-yr return periods by month of year and latitude, from the MERRA-2 AR chronology, water years 1981–2016. Gray cells in (a) are latitude–month combinations in which too few AR landfalls have occurred to allow 20-yr return period estimates.

to about 39°–41°N until about April when the largest maxima have returned to 40°–43°N.

Thus, generally, the most intense ARs have occurred in the PNW in autumn, arriving farther south as the wet season (October–March) continues, reaching as far south as northern California by early spring. By mid- to late spring, AR intensities generally decline, and by summer, ARs are weak enough to be of little practical consequence (e.g., Neiman et al. 2008; Rutz et al. 2014). This seasonality is in keeping with the overall frequencies of cool-season AR landfalls reported by Rutz et al. (2014). This seasonal evolution of AR IVT maxima corresponds to the general southward migration of North Pacific storm tracks from autumn into winter, followed by the weakening and retreat of the storm track back to the north again with the coming of summer (Cayan and Roads 1984). In addition to this storm-track seasonality, it is possible that the late summer to early autumn entrance of tropical cyclones and other tropical moisture exports (Knippertz and Wernli 2010) into western parts of the North Pacific basin provides added moisture that ARs can entrain, increasing the chances for particularly strong ARs to form in that season. This is when the storm track is focused, and the strongest West Coast ARs arrive, in the Pacific Northwest (Fig. 9). Thus, some of the overall dominance of PNW ARs over all others along the West Coast may reflect this temporal convergence of tropical moisture deliveries to the North Pacific basin and the most opportune storm-track location for PNW storminess.

8. Conclusions

Atmospheric rivers come in all sizes and strengths. Modest ARs can be characterized by comparison to other ARs in terms of their ranks within simple percentiles of all past ARs at a given location. Stronger AR intensities are categorized here in terms of return periods or, equivalently, historically estimated probabilities that at least one AR will exceed a given IVT threshold in any given year. Using a 1980–2016 chronology of AR landfalls on the U.S. West Coast derived from the MERRA-2 dataset, the largest and rarest instantaneous AR IVTs have occurred between about 41° and 46°N, with maximum IVTs declining to the north and, especially, to the south. This same general pattern applies to IVT maxima at all return periods longer than one year. The historically largest annual-maximum storm-sequence IVT totals (the IVT rates temporally integrated over the entire time that a continuous sequence of AR conditions is present overhead) have occurred around 42.5°N, with significant scatter among the largest few events. Notably, the specific magnitudes of IVT totals in these large storm sequences derive mostly from their long durations, rather than from the extremity of the IVTs that go into them. In autumn, maximum AR intensities are largest in the Pacific Northwest, and then through the winter and early spring the largest IVT rates occur farther south, reaching 39°–41°N by early spring, in keeping with the seasonal progression of the northeast Pacific storm track, before IVT maxima decline from spring into summer.

The patterns of annual-maximum IVTs in landfalling ARs reported here provide a clear perspective regarding the likelihoods of repeats of the more intense AR storms along the U.S. West Coast, geographically and seasonally. The bootstrap estimation-error analyses and the analyses of nonstationarities in the MERRA-2 IVTs reported here suggest that error bars of about ±10% may be desirable in reporting. Because AR precipitation intensities and totals from AR storms depend directly (albeit not solely) on IVT rates and totals (e.g., Neiman et al. 2002, 2009; Ralph et al. 2013; Guan and Waliser 2015), the historical return periods of maximum IVT rates offer a useful means for characterizing AR storms and the risks they pose. Graphical representations of IVT return periods reported here might be useful for characterizing and communicating relative AR strengths in observations, forecasts, and climate projections.

Acknowledgments. We are grateful for helpful comments from Chris Konrad (USGS) and three anonymous reviewers that improved this paper markedly. M.D.'s research was supported by the U.S. Geological Survey's Earth System Processes Division, Water Cycle Branch, and a cooperative arrangement with Sonoma County Water Agency. F.M.R.'s contributions at the Center for Western Weather and Water Extremes (CW^3E) were supported by the California Department of Water Resources and by the U.S. Army Corps of Engineers (USACE) Engineer Research and Development Center–Cooperative Ecosystem Studies Unit (CESU) as part of Forecast Informed Reservoir Operations (FIRO) under Grant W912HZ-15-2-0019. The AR and IVT chronologies used in this study can be obtained from http://www.inscc.utah.edu/~rutz/ar_catalogs/.

REFERENCES

Barth, N. A., G. Villarini, M. A. Nayak, and K. White, 2017: Mixed populations and annual flood frequency estimates in the western United States. *Water Resour. Res.*, **53**, 257–269, https://doi.org/10.1002/2016WR019064.

Brown, J. D., L. Wu, M. He, S. Regonda, H. Lee, and D.-J. Seo, 2014: Verification of temperature, precipitation, and streamflow forecasts from the NOAA/NWS Hydrologic Ensemble Forecast Service (HEFS): 1. Experimental design and forcing verification. *J. Hydrol.*, **519**, 2869–2889, https://doi.org/10.1016/j.jhydrol.2014.05.028.

Carpenter, J., and J. Bithell, 2000: Bootstrap confidence intervals: When, which, what? A practical guide for medical statisticians. *Stat. Med.*, **19**, 1141–1164, https://doi.org/10.1002/(SICI)1097-0258(20000515)19:9<1141::AID-SIM479>3.0.CO;2-F.

Cayan, D. R., and J. O. Roads, 1984: Local relationships between United States West Coast precipitation and monthly mean circulation parameters. *Mon. Wea. Rev.*, **112**, 1276–1282, https://doi.org/10.1175/1520-0493(1984)112<1276:LRBUSW>2.0.CO;2.

Compo, G. P., and Coauthors, 2011: The Twentieth Century Reanalysis Project. *Quart. J. Roy. Meteor. Soc.*, **137**, 1–28, https://doi.org/10.1002/qj.776.

Cordeira, J. M., F. M. Ralph, and B. J. Moore, 2013: The development and evolution of two atmospheric rivers in proximity to western North Pacific tropical cyclones in October 2010. *Mon. Wea. Rev.*, **141**, 4234–4255, https://doi.org/10.1175/MWR-D-13-00019.1.

——, ——, A. Martin, N. Gaggini, R. Spackman, P. Neiman, J. Rutz, and R. Pierce, 2017: Forecasting atmospheric rivers during CalWater 2015. *Bull. Amer. Meteor. Soc.*, **98**, 449–459, https://doi.org/10.1175/BAMS-D-15-00245.1.

Dee, D. P., and Coauthors, 2011: The ERA-Interim reanalysis: Configuration and performance of the data assimilation system. *Quart. J. Roy. Meteor. Soc.*, **137**, 553–597, https://doi.org/10.1002/qj.828.

Dettinger, M. D., 2013: Atmospheric rivers as drought busters on the U.S. West Coast. *J. Hydrometeor.*, **14**, 1721–1732, https://doi.org/10.1175/JHM-D-13-02.1.

——, and B. L. Ingram, 2013: The coming megafloods. *Sci. Amer.*, **308**, 64–71, https://doi.org/10.1038/scientificamerican0113-64.

——, F. M. Ralph, T. Das, P. J. Neiman, and D. Cayan, 2011: Atmospheric rivers, floods, and the water resources of California. *Water*, **3**, 445–478, https://doi.org/10.3390/w3020445.

Florsheim, J., and M. Dettinger, 2015: Promoting atmospheric-river and snowmelt fueled biogeomorphic processes by restoring river-floodplain connectivity in California's Central Valley. *Geomorphic Approaches to Integrated Floodplain Management of Lowland Fluvial Systems in North America and Europe*, P. Hudson and H. Middelkoop, Eds., Springer, 119–141, https://doi.org/10.1007/978-1-4939-2380-9_6.

Gelaro, R., and Coauthors, 2017: The Modern-Era Retrospective Analysis for Research and Applications, version 2 (MERRA-2). *J. Climate*, **30**, 5419–5454, https://doi.org/10.1175/JCLI-D-16-0758.1.

Gershunov, A., T. Shulgina, F. M. Ralph, D. A. Lavers, and J. J. Rutz, 2017: Assessing the climate-scale variability of atmospheric rivers affecting western North America. *Geophys. Res. Lett.*, **44**, 7900–7908, https://doi.org/10.1002/2017GL074175.

Ghil, M., and P. Malanotte-Rizzoli, 1991: Data assimilation in meteorology and oceanography. *Advances in Geophysics*, Vol. 33, Academic Press, 141–266, https://doi.org/10.1016/S0065-2687(08)60442-2.

GMAO, 2015: MERRA-2 inst3_3d_asm_Np: 3d, 3-hourly, instantaneous, pressure-level, assimilation, assimilated meteorological fields V5.12.4. GES DISC, accessed 30 July 2018, https://doi.org/10.5067/QBZ6MG944HW0.

Guan, B., and D. E. Waliser, 2015: Detection of atmospheric rivers: Evaluation and application of an algorithm for global studies. *J. Geophys. Res. Atmos.*, **120**, 12 514–12 535, https://doi.org/10.1002/2015JD024257.

——, and ——, 2017: Atmospheric rivers in 20 year weather and climate simulations: A multimodel, global evaluation. *J. Geophys. Res. Atmos.*, **122**, 5556–5581, https://doi.org/10.1002/2016JD026174.

——, N. P. Molotch, D. E. Waliser, E. J. Fetzer, and P. J. Neiman, 2010: Extreme snowfall events linked to atmospheric rivers and surface air temperature via satellite measurements. *Geophys. Res. Lett.*, **37**, L20401, https://doi.org/10.1029/2010GL044696.

——, D. E. Waliser, and F. M. Ralph, 2018: An intercomparison between reanalysis and dropsonde observations of the total water vapor transport in individual atmospheric rivers. *J. Hydrometeor.*, **19**, 321–337, https://doi.org/10.1175/JHM-D-17-0114.1.

Interagency Advisory Committee on Water Data, 1982: Guidelines for determining flood flow frequency. Bulletin 17B of the Hydrology Subcommittee, 183 pp., https://www.fema.gov/media-library/assets/documents/8403.

Kalnay, E., and Coauthors, 1996: The NCEP/NCAR 40-Year Reanalysis Project. *Bull. Amer. Meteor. Soc.*, **77**, 437–471, https://doi.org/10.1175/1520-0477(1996)077<0437:TNYRP>2.0.CO;2.

Knippertz, P., and H. Wernli, 2010: A Lagrangian climatology of tropical moisture exports to the Northern Hemisphere extratropics. *J. Climate*, **23**, 987–1003, https://doi.org/10.1175/2009JCLI3333.1.

Konrad, C. P., and M. D. Dettinger, 2017: Flood runoff in relation to water vapor transport by atmospheric rivers over the western United States, 1949–2015. *Geophys. Res. Lett.*, **44**, 11 456–11 462, https://doi.org/10.1002/2017GL075399.

Lamjiri, M. A., M. D. Dettinger, F. M. Ralph, and B. Guan, 2017: Hourly storm characteristics along the U.S. West Coast: Role of atmospheric rivers in extreme precipitation. *Geophys. Res. Lett.*, **44**, 7020–7028, https://doi.org/10.1002/2017GL074193.

Lavers, D. A., F. M. Ralph, D. E. Waliser, A. Gershunov, and M. D. Dettinger, 2015: Climate change intensification of horizontal vapor transport in CMIP5. *Geophys. Res. Lett.*, **42**, 5617–5625, https://doi.org/10.1002/2015GL064672.

Levene, H., 1960: Robust tests for equality of variances. *Contributions to Probability and Statistics: Essays in Honor of Harold Hotelling*, I. Olkin et al., Eds., Stanford University Press, 278–292.

Makkonen, L., 2006: Plotting positions in extreme value analysis. *J. Appl. Meteor. Climatol.*, **45**, 334–340, https://doi.org/10.1175/JAM2349.1.

Moore, B. J., P. J. Neiman, F. M. Ralph, and F. E. Barthold, 2012: Physical processes associated with heavy flooding rainfall in Nashville, Tennessee, and vicinity during 1–2 May 2010: The role of an atmospheric river and mesoscale convective systems. *Mon. Wea. Rev.*, **140**, 358–378, https://doi.org/10.1175/MWR-D-11-00126.1.

Neiman, P. J., F. M. Ralph, A. B. White, D. E. Kingsmill, and P. O. Persson, 2002: The statistical relationship between upslope flow and rainfall in California's coastal mountains: Observations during CALJET. *Mon. Wea. Rev.*, **130**, 1468–1492, https://doi.org/10.1175/1520-0493(2002)130<1468:TSRBUF>2.0.CO;2.

——, ——, G. A. Wick, J. D. Lundquist, and M. D. Dettinger, 2008: Meteorological characteristics and overland precipitation impacts of atmospheric rivers affecting the West Coast of North America based on eight years of SSM/I satellite observations. *J. Hydrometeor.*, **9**, 22–47, https://doi.org/10.1175/2007JHM855.1.

——, A. B. White, F. M. Ralph, D. J. Gottas, and S. I. Gutman, 2009: A water vapour flux tool for precipitation forecasting. *Proc. Inst. Civ. Eng.: Water Manage.*, **162**, 83–94, https://doi.org/10.1680/wama.2009.162.2.83.

——, L. J. Schick, F. M. Ralph, M. Hughes, and G. A. Wick, 2011: Flooding in western Washington: The connection to atmospheric rivers. *J. Hydrometeor.*, **12**, 1337–1358, https://doi.org/10.1175/2011JHM1358.1.

Oakley, N. S., J. T. Lancaster, M. L. Kaplan, and F. M. Ralph, 2017: Synoptic conditions associated with cool-season post-fire debris flows in the Transverse Ranges of southern California. *Nat. Hazards*, **88**, 327–354, https://doi.org/10.1007/s11069-017-2867-6.

——, ——, B. J. Hatchett, J. Stock, F. M. Ralph, S. C. Roj, and S. Lukashov, 2018: A 22-yr climatology of cool season hourly precipitation conducive to shallow landslides in California. *Earth Interact.*, **22**, https://doi.org/10.1175/EI-D-17-0029.1.

Ralph, F. M., and M. D. Dettinger, 2011: Storms, floods and the science of atmospheric rivers. *Eos, Trans. Amer. Geophys. Union*, **92**, 265–266, https://doi.org/10.1029/2011EO320001.

——, and ——, 2012: Historical and national perspectives on extreme West Coast precipitation associated with atmospheric rivers during December 2010. *Bull. Amer. Meteor. Soc.*, **93**, 783–790, https://doi.org/10.1175/BAMS-D-11-00188.1.

——, P. J. Neiman, and G. A. Wick, 2004: Satellite and CALJET aircraft observations of atmospheric rivers over the eastern North Pacific Ocean during the El Niño winter of 1997/98. *Mon. Wea. Rev.*, **132**, 1721–1745, https://doi.org/10.1175/1520-0493(2004)132<1721:SACAOO>2.0.CO;2.

——, ——, ——, S. Gutman, M. Dettinger, D. Cayan, and A. B. White, 2006: Flooding on California's Russian River: Role of atmospheric rivers. *Geophys. Res. Lett.*, **33**, L13801, https://doi.org/10.1029/2006GL026689.

——, T. Coleman, P. J. Neiman, R. J. Zamora, and M. D. Dettinger, 2013: Observed impacts of duration and seasonality of atmospheric-river landfalls on soil moisture and runoff in coastal northern California. *J. Hydrometeor.*, **14**, 443–459, https://doi.org/10.1175/JHM-D-12-076.1.

——, and Coauthors, 2017a: Atmospheric rivers emerge as a global science and applications focus. *Bull. Amer. Meteor. Soc.*, **98**, 1969–1973, https://doi.org/10.1175/BAMS-D-16-0262.1.

——, and Coauthors, 2017b: Dropsonde observations of total integrated water vapor transport within North Pacific atmospheric rivers. *J. Hydrometeor.*, **18**, 2577–2596, https://doi.org/10.1175/JHM-D-17-0036.1.

Rutz, J. J., W. J. Steenburgh, and F. M. Ralph, 2014: Climatological characteristics of atmospheric rivers and their inland penetration over the western United States. *Mon. Wea. Rev.*, **142**, 905–921, https://doi.org/10.1175/MWR-D-13-00168.1.

Shepard, M., 2015: What does a '100 or 1000-year' rain event actually mean? Forbes, 5 October, https://www.forbes.com/sites/marshallshepherd/2015/10/05/what-does-a-100-or-1000-year-flood-actually-mean/#6c6ce5601fb4.

Shields C. A., and Coauthors, 2018: Atmospheric River Tracking Method Intercomparison Project (ARTMIP): Project goals and experimental design. *Geosci. Model Dev.*, **11**, 2455–2474, https://doi.org/10.5194/gmd-11-2455-2018.

Young, A. M., K. T. Skelly, and J. M. Cordeira, 2017: High-impact hydrologic events and atmospheric rivers in California: An investigation using the NCEI Storm Events Database. *Geophys. Res. Lett.*, **44**, 3393–3401, https://doi.org/10.1002/2017GL073077.

Zhu, Y., and R. E. Newell, 1998: A proposed algorithm for moisture fluxes from atmospheric rivers. *Mon. Wea. Rev.*, **126**, 725–735, https://doi.org/10.1175/1520-0493(1998)126<0725:APAFMF>2.0.CO;2.